Article

Electrospun Carbon Nanotube-Based Scaffolds Exhibit High Conductivity and Cytocompatibility for Tissue Engineering Applications

Taylor C. Suh, Jack Twiddy, Nasif Mahmood, Kiran M. Ali, Mostakima M. Lubna, Philip D. Bradford, Michael A. Daniele, and Jessica M. Gluck*

Read Online

ACCESS | Metrics & More | Article Recommendations | Supporting Information

ABSTRACT: Carbon nanotubes (CNTs) are known for their excellent conductive properties. Here, we present two novel methods, "sandwich" (sCNT) and dual deposition (DD CNT), for incorporating CNTs into electrospun polycaprolactone (PCL) and gelatin scaffolds to increase their conductance. Based on CNT percentage, the DD CNT scaffolds contain significantly higher quantities of CNTs than the sCNT scaffolds. The inclusion of CNTs increased the electrical conductance of scaffolds from 0.0 ± 0.00 kS (non-CNT) to 0.54 ± 0.10 kS (sCNT) and 5.22 ± 0.49 kS (DD CNT) when measured parallel to CNT arrays and to 0.25 ± 0.003 kS (sCNT) and 2.85 ± 1.12 (DD CNT) when measured orthogonally to CNT arrays. The inclusion of CNTs increased

fiber diameter and pore size, promoting cellular migration into the scaffolds. CNT inclusion also decreased the degradation rate and increased hydrophobicity of scaffolds. Additionally, CNT inclusion increased Young's modulus and failure load of scaffolds, increasing their mechanical robustness. Murine fibroblasts were maintained on the scaffolds for 30 days, demonstrating high cytocompatibility. The increased conductivity and high cytocompatibility of the CNT-incorporated scaffolds make them appropriate candidates for future use in cardiac and neural tissue engineering.
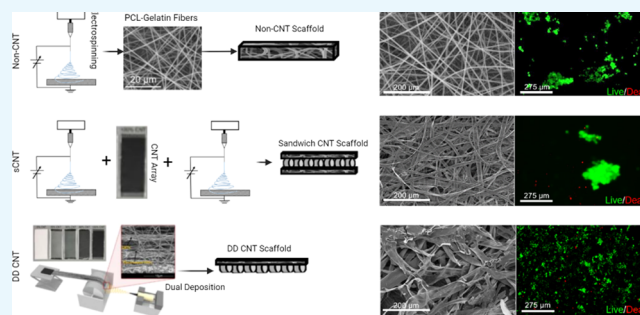
1. INTRODUCTION

Heart disease was the leading cause of death in the U.S. in 2020,[1] a statistic that has remained unchanged for the past 95 years.[2] Cardiac tissue engineering offers promising treatments and investigative tools for these cardiac diseases and disorders, including cell-based pacemakers,[3] cardiac patches,[4] microfluidic "heart-on-a-chip" models,[5] and regenerative therapies.[6] Additionally, many are hopeful for the possibility of engineering cardiac constructs capable of being implanted in lieu of heart transplants, which are insufficient due to massive donor shortages[7,8] and chronic immunogenic complications.[9−11] Similar to cardiac tissue engineering, advances in neural tissue engineering show promise in spinal cord nerve regeneration,[12,13] peripheral nerve regeneration,[14−16] and microfluidic "brain-on-a-chip" models for high-throughput testing and disease modeling.[17]

Because both cardiac and neural physiology depend on the electrical conduction of action potentials, conductive scaffolds are a common theme in tissue engineering research. In neural tissue engineering, chitosan−gelatin scaffolds doped with conductive hyaluronic acid-poly(3,4-ethylenedioxythiophene) (PEDOT) nanoparticles were shown to enhance neural stem cell proliferation and differentiation into neurons and astrocytes.[18] Researchers have also explored polyaniline[19,20]

and polypyrrole[21,22] to endow neural tissue engineering scaffolds with conductive properties. In cardiac tissue engineering, conductive scaffolds could be used to electrophysiologically mature human-induced pluripotent stem cell-derived cardiomyocytes (hiPSC-CMs). The immaturity of hiPSC-CMs compared to functional cardiomyocytes presents a roadblock to their use in cardiac tissue engineering due to the increased risk of introducing arrhythmias and the potential for poor electrical coupling with native tissues.[10,23] To address this limitation, researchers have attempted to electrophysiologically mature hiPSC-CMs using long-term culture,[24] electromechanical manipulations,[25] electrical stimulation,[25−27] protein regulation,[28] and co-culture with sympathetic neurons.[29] While successful, these approaches lack the microenvironmental control provided by a scaffold-based approach, particularly electrospinning, which allows selection of the material and
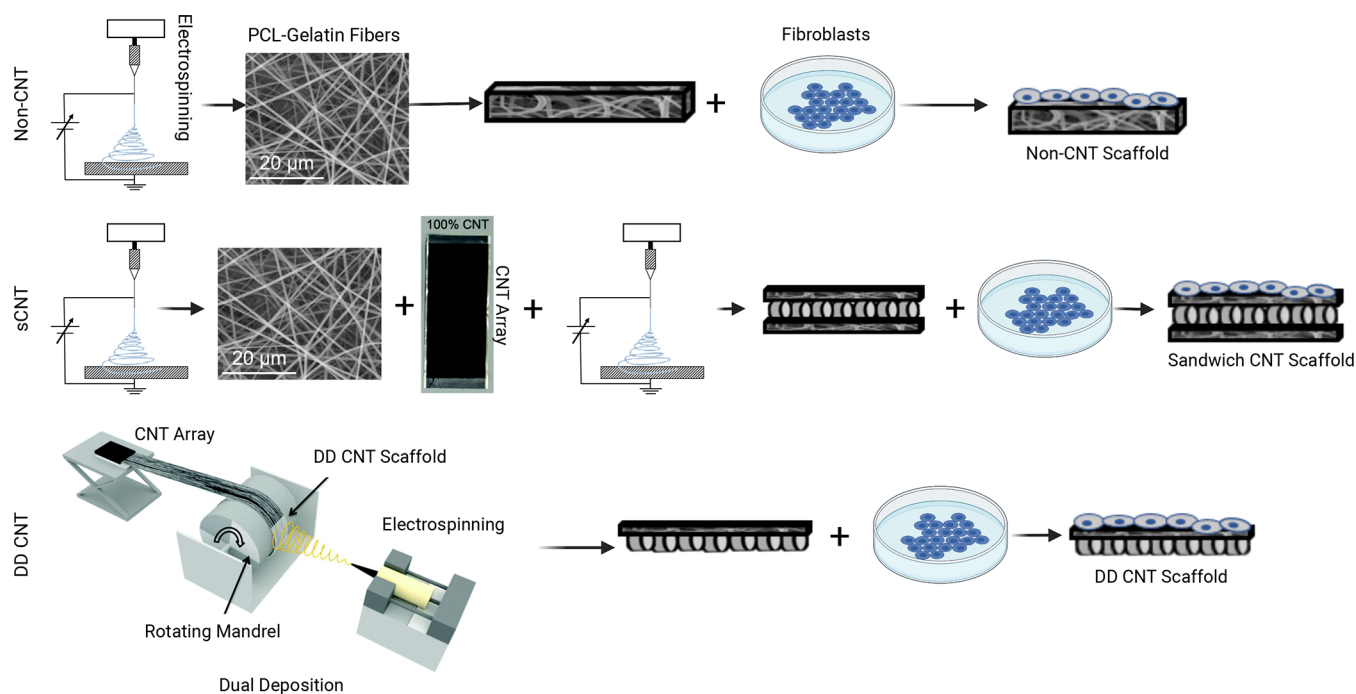
Figure 1. Schematic portraying the fabrication of scaffolds. (A) Non-CNT scaffolds are electrospun from PCL and gelatin. (B) "Sandwich" CNT (sCNT) scaffolds are electrospun, CNT arrays are manually stretched over electrospun fibers, and another layer is electrospun. (C) Dual deposition CNT (DD CNT) scaffolds are fabricated by winding CNTs and then electrospinning fibers onto the same rotating collector. Cells are seeded onto all three scaffold types.

control over morphology. Additionally, these approaches would be impossible to utilize *in vivo*, unlike a scaffold, which could be implanted. Thus, there remains a knowledge gap regarding the ability of conductive scaffolds to mature hiPSC-CMs. Studies suggest that a similar roadblock exists for the use of iPSC-derived neurons for neural tissue engineering. Transplantation of iPSC-derived neurons into murine cortices failed to generate action potentials within 7 weeks.[30] This indicates that iPSC-derived neurons similarly exhibit electrophysiological immaturity by default and could thus benefit from conductive scaffolds to mature them for neural tissue engineering applications.

We aim to endow scaffolds with conductivity by incorporating carbon nanotubes (CNTs) into electrospun polycaprolactone (PCL)−gelatin fibers. Electrospinning is ideal for the fabrication of scaffolds due to its production of fibers on the nano- to microscale, resulting in biomimicry of *in vivo* extracellular matrices (ECMs).[31] Additionally, electrospinning offers a high degree of morphological tunability based on solution properties and electrospinning parameters.[31−35] Finally, electrospun fibers are amenable to doping, coating, and post-processing, allowing for functionalization of scaffolds for specific tissue engineering needs.[36] We selected PCL due to its high biocompatibility and excellent mechanical properties[37] and gelatin due to its broad biocompatibility, promotion of cell adhesion, and cost-effectiveness.[38] Gelatin lacks the mechanical strength and elasticity typically desired for tissue engineering scaffolds and degrades too rapidly *in vivo* for cardiac and neural tissue engineering.[39] Conversely, PCL has excellent mechanical properties and takes longer to degrade, up to 2−3 years compared to gelatin, which can degrade within days.[37,40,41] By using PCL−gelatin scaffolds, we tune the degradation profile and provide enhanced mechanical properties. However, PCL−gelatin scaffolds remain electrically nonconductive.

We thus endowed these PCL−gelatin scaffolds with CNTs to confer conductive properties, as CNTs are well known for their superior electrical conductivity. Due to this electrical conductivity, CNTs have been shown to promote differentiation and maturity of neural stem cells when formed into rope-like substrates and used to deliver electrical stimulation,[42] enhance neurons' electrical activity when used as direct substrates,[43] and improve proliferation and neural differentiation of mesenchymal stem cells when loaded into electrospun scaffolds.[44] Additionally, thin films of CNTs functionalized with hydroxyl acid have been shown to enhance both cardiac and neuronal differentiation of canine iPSC-CMs.[45] Both mature cardiac and neuronal cells utilize electrophysiological signaling to propagate action potentials critical to their function. The ability of CNTs to enhance both cardiac and neuronal differentiation within canine iPSC-CMs suggests an underlying electrical mechanism. In addition to their conductive properties, the photoacoustic properties of CNTs have proven useful in neural tissue engineering. These photoacoustic properties have been shown to enable light-triggered depolarization of neurons without the need for genetic manipulation (such as the case in optogenetics), as well as to enhance neurite outgrowth.[46]

CNTs enhance mechanical robustness in addition to conferring electrical conductivity. Experiments by Liu et al. revealed that CNTs increased Young's modulus of electrospun poly(lactic-co-glycolic acid) scaffolds by 86% and tensile strength by 28% at a mere 0.5% concentration.[47] Additionally, CNTs have been shown to improve cellular adhesion[48,49] and confer antimicrobial properties.[50,51] The cytocompatibility of CNTs with human cells is controversial due to seemingly conflicting data and differing metrics. In prior work, CNTs have been claimed to be cytocompatible based on the lack of cytotoxicity toward Schwann cells on CNT substrates.[52]

Others have argued that CNTs are not cytocompatible due to studies observing the loss of cell viability in immortalized human epidermal keratinocytes following exposure to unrefined CNTs.[53] It has been more recently argued that the degree of CNT toxicity depends on many factors, including purity, dispersal, and fiber length.[54] Recent research has shown that the structure, diameter, and length of CNTs affect their pulmonary toxicity and cytotoxicity. It has been proven that bent multiwalled CNTs (MWCNTs) exhibit less cytotoxicity than straight MWCNTs, and that cytotoxicity of submicron-diameter carbon fibers increases with decreasing diameter and decreases with decreasing length.[55]

In this work, we endeavored to incorporate CNTs into electrospun PCL−gelatin scaffolds to take advantage of their superior conductive and mechanical properties and to demonstrate their cytocompatibility, thus providing a basis for their use as conductive scaffolds in cardiac and neural tissue engineering applications. We incorporated CNTs into our electrospun PCL−gelatin scaffolds using two distinct methods: "sandwich" and dual deposition. Here, we compare the CNT content, morphology, mechanical properties, degradation profiles, hydrophobicity, electrical conductance, and cytocompatibility of the scaffolds.

2. MATERIALS AND METHODS

2.1. Scaffold Fabrication. Polycaprolactone (PCL) (M_n = 90 g/mol, Sigma-Aldrich) was combined with type-A gelatin from porcine skin (gel strength ∼300 g Bloom, Sigma-Aldrich) in a 1:1 ratio and dissolved in 1,1,2,3,3,3-hexafluoro-1-propene (HFP) (Thermo Fisher) at 20% w/v concentration. During electrospinning, the solution was extruded at 4 mL/h and 14 kV was applied. The resultant electrospun PCL−gelatin fibers were collected onto copper shim with a 15 cm die−collector distance (Figure 1A).

Spinnable, vertically aligned MWCNTs were grown in a tube furnace using a modified version of the chlorine-mediated chemical vapor deposition (CVD) route.[56] The MWCNT arrays were grown on a quartz substrate at 760 °C with acetylene as the carbon precursor and $FeCl_2$ (anhydrous 99.5%, VWR) as the catalyst. At 760 °C, acetylene gas (99.5%, Machine and Welding Supply Company) was flowed at 600 sccm, chlorine gas (99.99%, Custom Gas Solutions) at 2 sccm, and carrier gas argon (99.999%, Machine and Welding Supply Company) at 398 sccm, while the system pressure was regulated at 5 Torr. The acetylene gas flow was stopped after 20 min from the start of the growth process, and the grown arrays were left in the argon and chlorine flow for 20 additional min. The system was then purged with argon during cooling. A detailed procedure of this CVD CNT growth method was previously published by the Bradford group.[57] The resultant MWCNTs exhibited an average diameter of 39 ± 6 nm (measured by a field emission scanning electron microscope), an average length of 1 mm (measured by an optical microscope), an aspect ratio of ∼25,650, and a purity of 99.67% (measured by TGA; only 0.33% iron oxide catalyst residue materials left after 900 °C air oxidation). Notably, 1 mm is longer than most MWCNTs.

CNT arrays were formed by drawing horizontally aligned CNT sheets from the vertically aligned MWCNT arrays, thus drawing a small bundle of nanotubes at the edge of a spinnable array to continuously transform vertically aligned MWCNTs into horizontally aligned MWCNT sheets. Continuous collection of the aligned MWCNT sheets around a rotating mandrel resulted in a flat sheet with the desired thickness.

CNTs were incorporated into electrospun PCL−gelatin scaffolds using two distinct methods. In the "sandwich" CNT (sCNT) method, PCL and gelatin fibers were electrospun onto static copper shim. CNT arrays were manually stretched over electrospun fibers and then another layer was electrospun on top (Figure 1B). In the dual deposition CNT (DD CNT) method, the same CNT arrays from the "sandwich" method were wound onto a copper shim affixed to a mandrel rotating at approximately 20 RPM. CNT arrays were wound around the entire circumference of the rotating mandrel 2.5 times. PCL and gelatin fibers were electrospun onto the same rotating mandrel, depositing on top of the CNT arrays (Figure 1C).

2.2. CNT Volume Percent Quantification. For sCNT and DD CNT scaffolds, 1×1 cm^2 samples ($n = 10$ per scaffold type) were cut. Scaffold samples were momentarily dipped in HFP (Thermo Fisher) and initial wet weights were acquired. Samples were then immersed in HFP for 1 h to dissolve the PCL and gelatin components of the scaffolds, leaving behind only the CNT component. Final wet weights were then measured. Assuming that the density of the PCL−gelatin electrospun fibers and the density of CNT arrays are constant, the mass percent of CNTs within scaffolds is equivalent to the volume percent of CNTs within scaffolds.

2.3. Electron SEM Assessment of Morphology. For each scaffold type, 0.75×0.75 cm^2 samples ($n \geq 5$ per scaffold type) were cut. Samples were mounted with carbon adhesive onto SEM stubs and sputter-coated with 10 nm of gold and palladium and imaged with an electron microscope (Hitachi TM4000) at 10 kV. Three SEM images were taken of each sample, and 20 measurements of fiber diameter and pore size were taken for each image using ImageJ, an image analysis software freely available at imagej.nih.gov/ij. Mean fiber diameter and pore size were calculated, as well as fiber diameter and pore size distribution.

2.4. Quantification of Mechanical Properties Using the Modified Tensile Strip Test. For each scaffold type, 4×1 cm^2 samples ($n = 5$ for non-CNT and DD CNT, $n = 4$ for sCNT) were cut. Standard $3'' \times 5''$ index cards were cut into "C-cards" with a 2.54 cm gap for sample placement, into which samples were affixed between double-sided tape and lab tape (Supporting Figure 1A). The C-cards containing samples were placed into a tensile tester (MTS, Q-Test 5) using 2 N pinch clamp grips, and the C-card was partially cut to leave the samples between the grips (Supporting Figure 1B and 1C). Tensile strip tests were run using a 5 N load cell, 2.54 cm grip separation, 50% break sensitivity, and 0.01 mm/s strain rate. This procedure was adapted from the ASTM standard D5035, "Textile Strip Method." From the resultant measurements of sample extension (mm) and applied load (kN), Young's modulus for each sample was calculated.

2.5. Enzymatic Degradation by Weight. For each scaffold type, 0.5×0.5 cm^2 samples ($n = 10$ per scaffold type) were cut and placed into 12-well plates. The samples were immersed in a 1:1 solution of 0.25 mg/mL collagenase in 0.1 M Tris-HCl and 0.005 M $CaCl_2$ for the enzymatic degradation of gelatin and 0.0025 mg/mL *Pseudomonas lipase* (Type XIII, ≥15 units/mg solid, Millipore Sigma) in phosphate-buffered saline (PBS) for the enzymatic degradation of PCL. A 0.25 mg/mL collagenase concentration was used based on a modification of Alberti and Xu, who used a 1 mg/mL concentration of collagenase in 0.1 M Tris-HCl and 0.005
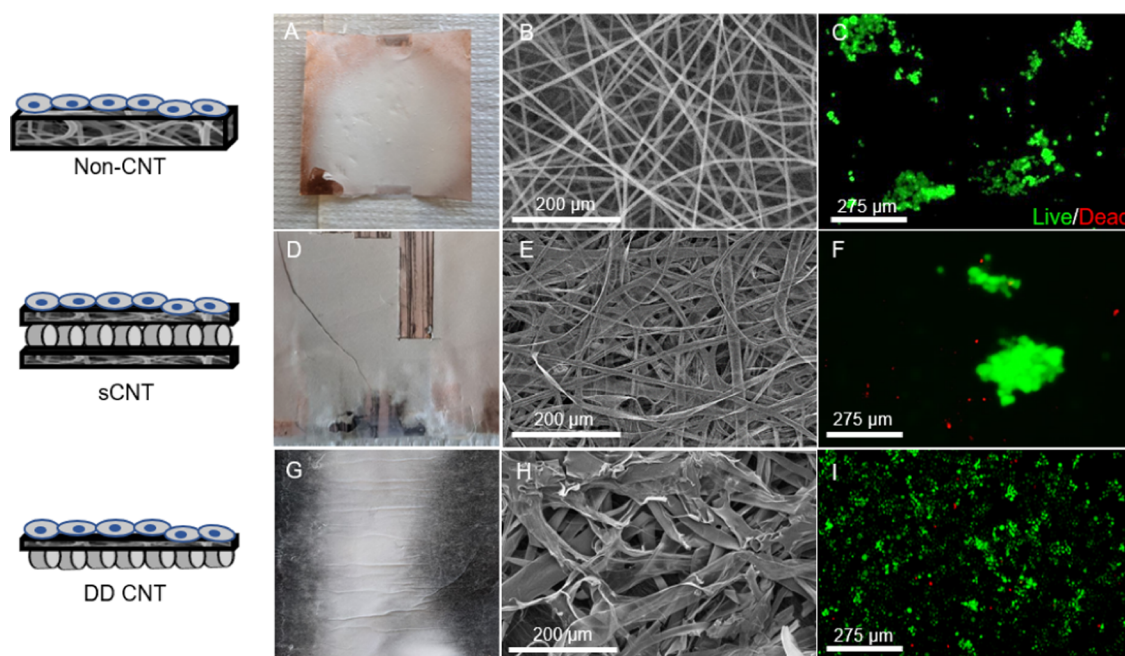
Figure 2. CNT incorporation into scaffolds. (A, D, G) Gross images of scaffolds. (B, E, H) SEM images of scaffolds. Scale bars = 200 μm. (C, F, I) LIVE/DEAD assays of NIH 3T3 cells on scaffolds 2 days post seeding. Scale bars = 275 μm.

M $CaCl_2$ to analyze degradation of tendon-derived collagen fibril-based tissue engineering scaffolds.[58] The concentration was reduced from 1 to 0.25 mg/mL collagenase because the electrospun scaffolds' microfibers are significantly smaller than the tendon-derived collagen fibrils studied by Alberti and Xu.[58] In 2018, Spearman et al.[59] employed *P. lipase* to increase the degradation rate of electrospun PCL/PCL−polyglycolide nanocomposite fibers via cleavage of PCL's ester bonds. Because the purpose of the present study was to analyze and not increase the degradation rate, the *P. lipase* concentration was reduced from 0.4 mg/mL used by Spearman et al. to 0.0025 mg/mL. The 12-well plates were kept in a heated chamber maintained at 37 °C for 4 weeks. Dry and wet weights were collected from six of the samples on days 0, 1, 7, 14, 21, and 28. Dry weights were acquired by weighing samples after they were desiccated overnight. Both dry and wet weights were collected to assess scaffolds under culture-like conditions (wet measurement) and to control for the effect of varying hydrophobicity on weight (dry measurement). Multiple SEM images were collected from one sample per each scaffold type on days 1, 7, 14, 21, and 28.

2.6. Contact Angle Measurement. For each scaffold type, 2.54 × 2.54 cm^2 samples ($n = 3$ per scaffold type) were cut. Contact angle with water droplets was measured using a goniometer (Dataphysics OCA System, FDS Corp).

2.7. Electrical Analysis. For each scaffold type, 0.75 × 0.75 cm^2 samples ($n = 10$ per scaffold type) were cut. End-to-end resistance was quantified using a handheld multimeter (True RMS Multimeter, Keysight) with probes placed on the edges of the samples either parallel or orthogonal to CNT arrays. For all scaffold types, the probes were placed onto the sides of the scaffolds on which the cells were later seeded. Conductance was calculated as the inverse of resistance.

2.8. Cell Culture. NIH 3T3 murine fibroblasts were maintained at 37 °C and 5% relative humidity and cultured in high-glucose DMEM media (Corning) supplemented with 10% fetal bovine serum (Atlas Biologicals) and 1% Penicillin−

Streptomycin (Fisher Scientific). Media changes occurred every other day.

NIH 3T3 cells were passaged and then seeded onto sterilized 1 × 1 cm^2 samples cut from each scaffold type at a density of 10^6 cells/cm^2, with 3 × 10^4 cells plated into a well without a scaffold as a control. Cellularized scaffolds were maintained in 1.5 mL each of DMEM media (Corning) supplemented with 10% fetal bovine serum (Atlas Biologicals) and 1% Penicillin−Streptomycin (Fisher Scientific).

2.9. Cytocompatibility Analyses. In preparation for the following cytocompatibility analyses, scaffolds were cut into 1 × 1 cm^2 samples and placed into 24-well plates. They were sterilized with 70% ethanol for 20 min, immersed in fresh PBS three times for 5 min each, and then stored in PBS at 4 °C overnight. The following day, a control well was coated with 0.1% gelatin in PBS. Cells were passaged and resuspended at 5 × 10^7 cells/mL, 20 μL of the cell suspension was slowly added to each scaffold, and the samples were incubated at 37 °C and 5% CO_2 for 1 h to allow for cell adhesion, after which 1 mL of the appropriate media was added to each well.

2.9.1. Live/Dead Assays. For a preliminary cytocompatibility analysis of all scaffold types, LIVE/DEAD viability assays (Invitrogen) were performed using NIH 3T3 murine fibroblasts. LIVE/DEAD assays were performed with 3T3 cells on days 2, 7, 14, 21, and 27 after seeding ($n \geq 3$ per scaffold type). Ten images were collected using a fluorescent microscope (EVOS FL Auto 2, Invitrogen), and cellularized scaffolds were returned to culture media. To determine viability, the quantity of live cells and dead cells for each image was determined using Celleste 5 software. Viability was then calculated as the fraction of live cells over total cells.

2.9.2. Proliferation Assays. Alamar Blue assesses cellular viability by quantifying fluorescence generated by resazurin as it reduces to resorufin upon entering living cells due to their enzymatic activity. On days 1, 3, 5, and 7 post seeding, 150 μL of Alamar Blue reagent (Fisher Scientific) was added to each well of a plate containing 3T3 cells seeded onto 1 × 1 cm^2

samples from each scaffold type (n = 3 per type) and one well with cells containing no scaffold as a control. The plate was incubated at 37 °C for 1 h. Following incubation, 100 μL of the media and reagent was added from each sample in triplicate to a 96-well plate. Fluorescence within the 96-well plate was quantified using a microplate reader (Synergy HT, BioTek) set to 540/25 λ excitation, 590/35 λ emission and maintained at 37 °C.

2.9.3. Immunocytochemistry. On day 14 post seeding, cellularized scaffold samples were fixed with 4% paraformaldehyde, permeabilized using 0.25% TritonX-100 in PBS and 0.1% Tween-20 in PBS, serum-blocked using 2% bovine serum albumin and 2% goat serum in 0.1% Tween-20 in PBS, stained with phalloidin, counterstained with Hoechst 33342, and imaged using a fluorescent microscope (EVOS FL Auto 2, Thermo Fisher).

To assess scaffold attachment and migration on CNT-based scaffolds (n = 3 per scaffold type), on day 7 post seeding, the cellularized scaffolds were fixed using 4% paraformaldehyde. Samples were paraffin-sectioned and placed onto slides. Following sectioning, the slides were deparaffinized and permeabilized using a SafeClear II xylene substitute (Fisher Scientific), a progression of decreasing ethanol concentrations in deionized water, 0.1% TritonX-100 in PBS, and 0.1% Tween-20 in PBS. Samples were then serum-blocked using 2% bovine serum albumin and 2% goat serum in 0.1% Tween-20 in PBS, stained with Hoechst 33342, and imaged on the DAPI channel of a fluorescent microscope (EVOS FL Auto 2, Invitrogen).

2.10. Statistical Analyses. Results are presented as mean $\pm$ standard error of the mean. Statistical significance was tested using analysis of variance (ANOVA). Probability values of $p <$ 0.05 were considered statistically significant.

3. RESULTS

3.1. CNTs can be Incorporated into Electrospun Scaffolds Using the "Sandwich" or the Dual Deposition Method. CNTs were successfully incorporated (Figure 2). The resultant scaffolds are shown with schematics, SEM images, and day 2 LIVE/DEAD assays using NIH 3T3 murine fibroblasts (Figure 2). From the visual analysis of the SEM images, it is evident that the CNTs are more evenly distributed in the DD CNT scaffolds (Figure 2H, Supporting Figures 2−4, Table 1) than in the sCNT scaffolds (Figure 2E, Supporting

Table 1. Mean Values $\pm$ Standard Error of the Mean for Volume Percent of CNTs Within Scaffolds; n = 10 per Scaffold Type

	non-CNT	sCNT	DD CNT
volume percent of CNTs (%)	$0.00 \pm 0.00^{a,c}$	$26.39 \pm 2.05^{a,b}$	$51.75 \pm 5.66^{b,c}$

*[a]*Denotes $p < 0.05$ significant difference between non-CNT and sCNT. *[b]*Denotes $p < 0.05$ significant difference between sCNT and DD CNT. *[c]*Denotes $p < 0.05$ significant difference between non-CNT and DD CNT.

Figures 2−4, Table 1). It is also evident from the greater presence of CNTs in SEM images that the CNT concentration is higher for DD CNT (Figure 2H) scaffolds than for sCNT (Figure 2E) scaffolds. These conclusions are both also apparent from gross visual analysis of the scaffolds (Figure 2A,D,G).
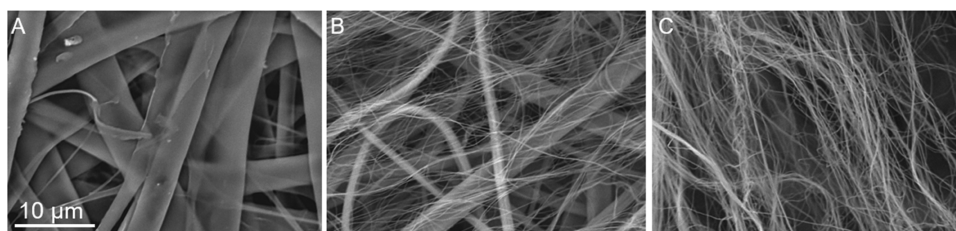
On day 2 post seeding, LIVE/DEAD assays performed using NIH 3T3 murine fibroblasts showed good cellular proliferation on all three scaffold types. For representative images of each scaffold type, there were 100% live and 0% dead cells for non-CNT scaffolds (Figures 2C), 95.48% live and 4.52% dead for sCNT scaffolds (Figure 2F), and 98.55% live and 1.45% dead for DD CNT scaffolds (Figure 2I). For all scaffold types, dead cells were far outnumbered by live cells, indicating no significant cytotoxicity. Notably, almost all cells formed clusters on sCNT (Figure 2F) scaffolds, with some cells forming clusters on non-CNT (Figure 2C) scaffolds, and no cluster formation on DD CNT (Figure 2I) scaffolds. This indicates that the sCNT scaffolds present a more heterogeneous microenvironment, wherein cells are more attracted to certain areas of the scaffold than others, migrating to and forming clusters within these areas.

3.2. Volume Percent of CNTs is Significantly Higher Within DD CNT Scaffolds than Within sCNT Scaffolds. As visible in high-magnification SEM images (Figure 3) and as quantified based on the volume percent of CNTs within scaffolds (Table 1), DD CNT scaffolds have the highest quantity of CNTs within them (51.75 $\pm$ 5.66%), followed by sCNT scaffolds (26.39 $\pm$ 2.05%). Non-CNT scaffolds, obviously, contain no CNTs (0.00 $\pm$ 0.00%). The differences in volume percent of CNTs are significant between all three groups.

3.3. Inclusion of CNTs Significantly Increases Fiber Diameter and Pore Size. The inclusion of CNTs via both sCNT and DD CNT methods significantly increased the mean fiber diameter of the resultant scaffolds from 1.05 $\pm$ 0.02 to 20.21 $\pm$ 0.92 μm (sCNT) and 39.53 $\pm$ 3.92 μm (DD CNT) (Table 1). The DD CNT method increased the fiber diameter significantly more than the "sandwich" method (Table 1). The inclusion of CNTs via both fabrication methods also significantly increased the mean pore size of the scaffolds (Tables 1 and 2).

3.4. Inclusion of CNTs Using "Sandwich" and Dual Deposition Methods Significantly Increased Both Mean Young's Modulus and Mean Failure Load of Scaffolds. Stress−strain curves show that sCNT and DD CNT scaffolds are stronger and more ductile with higher failure loads and Young's moduli, while non-CNT scaffolds are more brittle with lower failure loads and Young's moduli (Figure 4). Inclusion of CNTs using the "sandwich" and dual deposition methods significantly increased their Young's moduli from 6.47 $\pm$ 0.16 MPa (non-CNT) to 19.76 $\pm$ 1.95 MPa (sCNT) and 59.32 $\pm$ 6.40 MPa (DD CNT) (Figure 4B). This is equivalent to a 205.4 and 816.9% increase in Young's modulus for sCNT and DD CNT scaffolds, respectively. Thus, we conclude that inclusion of CNTs into our electrospun scaffolds significantly increased their Young's modulus, enhancing their mechanical robustness. A previous study reported that inclusion of CNTs into electrospun scaffolds yielded an 8% increase in the scaffolds' observed Young's modulus at an 0.25% CNT concentration and an 86% increase at an 0.5% concentration.[47] This is consistent with our results, as we used a significantly higher ratio of CNTs to electrospun fibers and thus achieved significantly higher Young's modulus. Additionally, inclusion of CNTs significantly increased the mean failure load of scaffolds from 0.13 $\pm$ 0.012 kN for non-CNT scaffolds to 0.33 $\pm$ 0.0002 kN for sCNT scaffolds and 0.38 $\pm$ 0.016 kN for DD CNT scaffolds (Figure 4C).

Figure 3. High-magnification SEM images of non-CNT (A), sCNT (B), and DD CNT (C) scaffolds exhibiting higher CNT content in DD CNT scaffolds than sCNT scaffolds and no CNTs in non-CNT scaffolds. Scale bars = 10 μm.

Table 2. Mean Values $\pm$ Standard Error of the Mean for Fiber Diameter and Pore Size, With Summaries of Their Distributions; n = 10 Per Scaffold Type for Mean Fiber Diameters and Pore Sizes and n = 4 With 160 Measurements Each Per Scaffold Type for Distribution Analyses

	non-CNT	sCNT	DD CNT
mean fiber diameter (μm)	$1.05 \pm 0.02^{a,c}$	$20.01 \pm 0.92^{a,b}$	$39.53 \pm 3.92^{b,c}$
fiber diameter distribution	unimodal, skewed right (Supporting Figure 3A)	unimodal, skewed right (Supporting Figure 4A)	unimodal, skewed right (Supporting Figure 5A)
mean pore size (μm^2)	$9.70 \pm 1.30^{a,c}$	$618.27 \pm 70.77^{a,b}$	$9778.36 \pm 1041.83^{b,c}$
pore size distribution	unimodal, skewed right (Supporting Figure 3B)	unimodal, skewed right (Supporting Figure 4B)	bimodal, skewed right (Supporting Figure 5B)

[a]Denotes $p < 0.05$ significant difference between non-CNT and sCNT. [b]Denotes $p < 0.05$ significant difference between sCNT and DD CNT. [c]Denotes $p < 0.05$ significant difference between non-CNT and DD CNT.
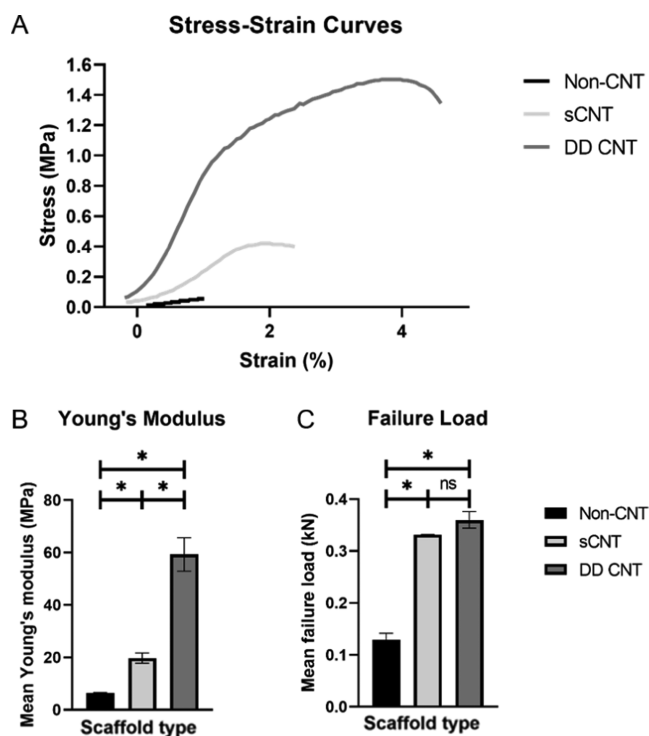

Figure 4. Mechanical characterization of scaffolds. (A) Representative stress–strain curves from one sample per scaffold type. (B) Mean Young's modulus. $n \geq 4$ for each scaffold type. (C) Mean failure load. $n \geq 4$ for each scaffold type. *Denotes $p < 0.05$ significant difference between groups. Black = non-CNT, light gray = sCNT, and dark gray = DD CNT.

3.5. Inclusion of CNTs Reduced the Enzymatic Degradation Rate As Quantified By Change in Wet and Dry Weights. Based on both mean dry (Figure 5A) and wet (Figure 5B) weights, non-CNT scaffolds exhibited the steepest degradation profile, followed by sCNT scaffolds, and

then DD CNT scaffolds. The CNTs remained visible in SEM images up to day 7 in sCNT scaffolds (Figure 5C,G) and up to day 28 in DD CNT scaffolds (Figure 5C,O).

3.6. Inclusion of CNTs Significantly Increased Water Contact Angle of Scaffolds. The inclusion of CNTs by both "sandwich" and dual deposition methods significantly increased the mean water contact angle of scaffolds from $73.2 \pm 0.9°$ for non-CNT scaffolds to $143.9 \pm 1.2°$ for sCNT scaffolds and $103.9 \pm 1.0°$ for DD CNT scaffolds. Hence, the non-CNT scaffolds were the most hydrophilic, followed by DD CNT scaffolds, and then sCNT scaffolds (Figure 6). Additionally, the sCNT scaffolds exhibited a significantly larger mean water contact angle than the DD CNT scaffolds.

3.7. Inclusion of CNTs Significantly Increased End-to-End Conductance of Scaffolds. CNT inclusion using the "sandwich" and dual deposition methods increased the end-to-end conductance of the scaffolds from 0.00 ± 0.00 kS (both parallel and orthogonal), with a greater increase in conductance for the DD CNT scaffolds (5.22 ± 0.49 kS parallel, 2.85 ± 1.12 kS orthogonal) than the sCNT scaffolds (0.54 ± 0.10 kS parallel, 0.25 ± 0.003 kS orthogonal) (Figure 7B). This increased conductance was significant for DD CNT scaffolds but not for sCNT scaffolds. The increased conductance in DD CNT scaffolds correlates to the excellent electrical conductivity of CNTs. The conductance increased more for DD CNT than for sCNT scaffolds because the dual deposition method yielded a higher volume percent of CNTs (Table 1) than the "sandwich" method.

The increased conductance in sCNT and DD CNT scaffolds exhibited anisotropy, with conductance becoming significantly higher when measured parallel to CNT arrays (0.54 kS sCNT, 5.22 kS DD CNT) compared to when measured orthogonal to CNT arrays (0.25 kS sCNT, 2.86 kS DD CNT) (Figure 7B). This anisotropy of conductance is directly correlated to the inherent geometric anisotropy of the embedded CNT networks, in which the fibers are aligned toward a particular axis.
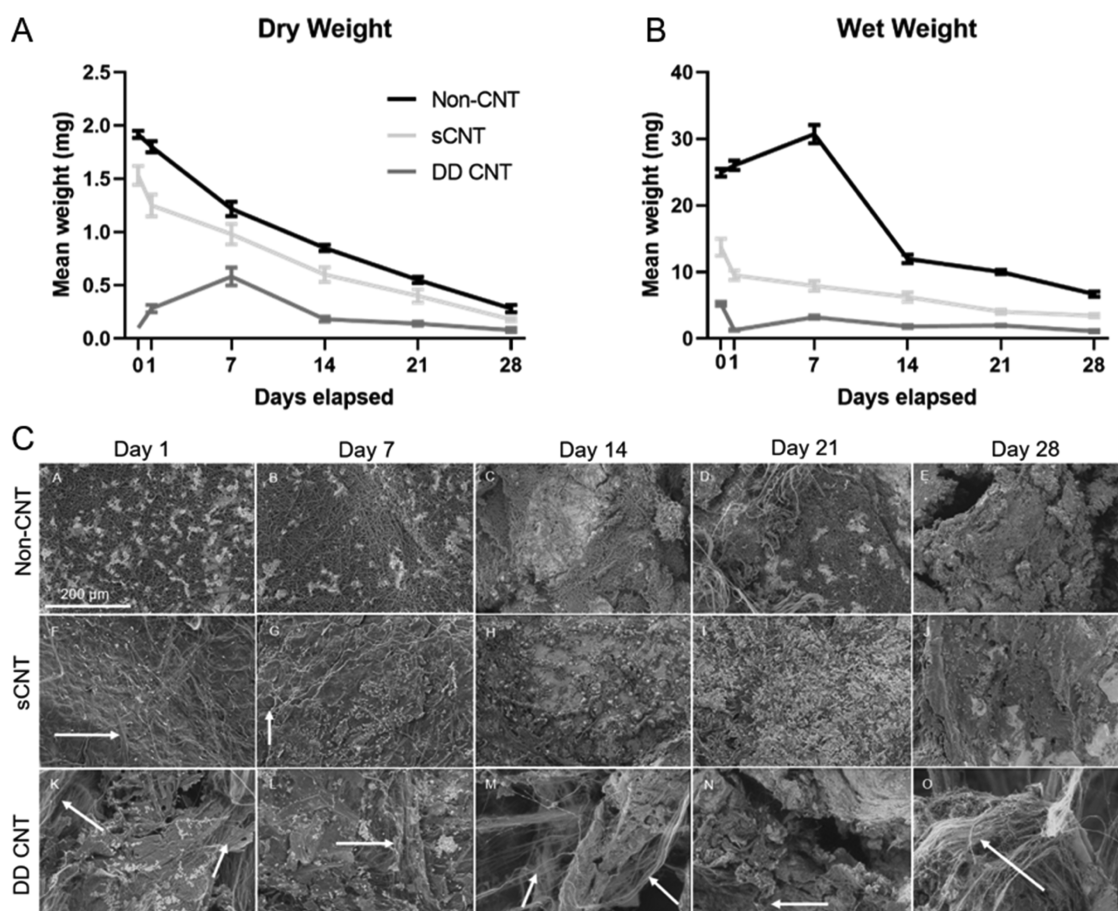
Figure 5. Degradation profiles of scaffolds exposed to collagenase and *P. lipase*. (A) Mean dry weight of scaffolds over 28 days. $n = 6$ per scaffold type. (B) Mean wet weights of scaffolds over 28 days. $n = 6$ per scaffold type. (C) SEM images of scaffolds over 28 days. CNTs indicated by arrows. $n = 1$ per scaffold type. Scale bars = 200 μm.
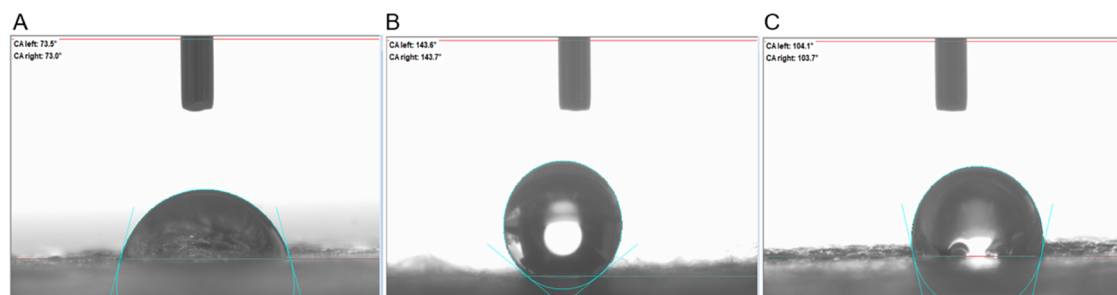

Figure 6. Water contact angle. Representative images of one sample per (A) non-CNT, (B) sCNT, and (C) DD CNT scaffold type. $n = 3$ per scaffold type.

3.8. All Scaffold Types Demonstrate Cytocompatibility With Murine Fibroblasts for Up To 1 Month Post Seeding. Based on fluorescent microscopy of the month-long progression of LIVE/DEAD assays using NIH 3T3 cells, all scaffold types demonstrated high cytocompatibility with minimal to no cytotoxicity (Figure 8). Cells attached and proliferated well to all scaffolds, both without CNTs (Figure 8A−E) and with CNTs incorporated via the "sandwich" (Figure 8F−J) and dual deposition (Figure 8K−O) methods. Visual observation revealed that the cells also successfully migrated through the layers of the scaffolds for all scaffold types, indicating a high degree of biointegration (Figure 8N) and suggesting that the scaffolds' structural microenvironment is physiologically favorable toward intravasation of the murine

fibroblasts. By day 28, based on quantities of cells observed in the images, the cells proliferated the most on the DD CNT scaffolds (Figure 8O), followed by the non-CNT scaffolds (Figure 8E), and then the sCNT scaffolds (Figure 8J).

Metabolic activity is a good indicator of cytocompatibility because it quantifies cellular proliferation. NIH 3T3 cells demonstrate excellent metabolic activity when seeded onto the scaffolds, with no significant difference in metabolic activity between cells seeded onto scaffolds vs without scaffolds nor the significant difference between cells seeded onto scaffolds with vs without CNTs (Figure 9). On days 1, 3, and 7 post seeding, there was no significant difference overall between Alamar Blue fluorescence (RFU) in all groups (non-CNT scaffolds, sCNT scaffolds, DD CNT scaffolds, and non-scaffold cell-only
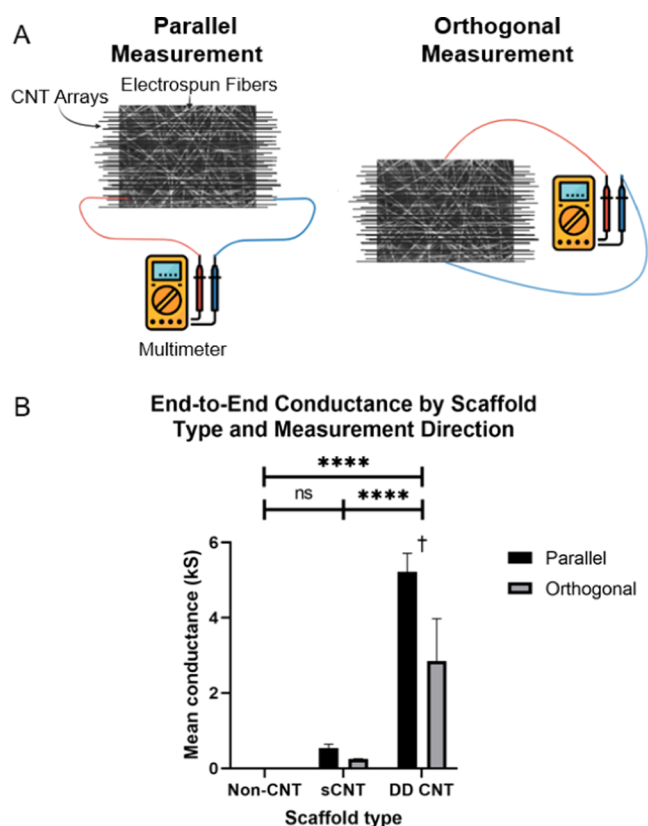
Figure 7. End-to-end conductance of scaffolds. (A) Measurement of end-to-end resistance parallel and orthogonal to CNT arrays. (B) Mean end-to-end conductance for electrospun scaffolds. $n = 10$ per scaffold type. *Denotes $p < 0.05$ significant difference between scaffold types and † denotes $p < 0.05$ significant difference between measurement directions. Black = non-CNT, light gray = sCNT, and dark gray = DD CNT.

viability. This is consistent with the visual assessment of LIVE/DEAD assays (Figure 9), which show the lowest rate of cellular proliferation on sCNT scaffolds, compared to non-CNT and DD CNT scaffolds, on both day 2 and day 7.

On day 14 post seeding, phalloidin and Hoechst 33342 staining (Figure 8) revealed that NIH 3T3 cells continued to attach and proliferate on scaffolds both without CNTs (Figure 8A) and with CNTs (Figure 9B,C). Furthermore, the morphology of the cells remained intact and unchanged, as indicated by the staining of actin filaments green and nuclei blue (Figure 9C). It is evident from the images that the cells attached to the sCNT (Figure 9B) and DD CNT (Figure 9C) scaffolds because cells are only located where the scaffolds are present, forming an "edge" within the images.

Sagittal sectioning was performed on cellularized scaffolds, thus allowing imaging of the cellularized scaffolds in cross section. From the staining of these sections, we observed that NIH 3T3 cells migrated into the microstructure of sCNT and DD CNT scaffolds with full-thickness penetration. Fibroblasts (indicated by their nuclei, stained blue with Hoechst 33342) on both sectioned sCNT (Figure 10A−B) and DD CNT (Figure 10C−D) scaffolds on day 7 post seeding migrated throughout the entire thickness of the scaffolds (Figure 10). Cells migrated more thoroughly on the sCNT scaffolds than on the DD CNT scaffolds, with 66.8% of cells migrating to the inner 50% of sCNT scaffolds, in contrast to only 42.4% of cells migrating to the inner 50% of DD CNT scaffolds. However, this is likely affected by the varying scaffold thicknesses; the sCNT scaffolds (Figure 10B) are thinner than the DD CNT scaffolds (Figure 10D).

4. DISCUSSION

The volume percent of CNTs within DD CNT scaffolds is significantly higher than within sCNT scaffolds. The volume percent of CNTs within both sCNT and DD CNT scaffolds is, obviously, significantly higher than within non-CNT scaffolds. The inclusion of CNTs into the scaffolds significantly increased both their fiber diameter (Figure 1A, Supporting Figures S2−S4) and pore size (Figure 1B, Supporting Figures S2−S4). The significant increase in scaffolds' mean fiber diameter when CNTs were incorporated is likely due to the
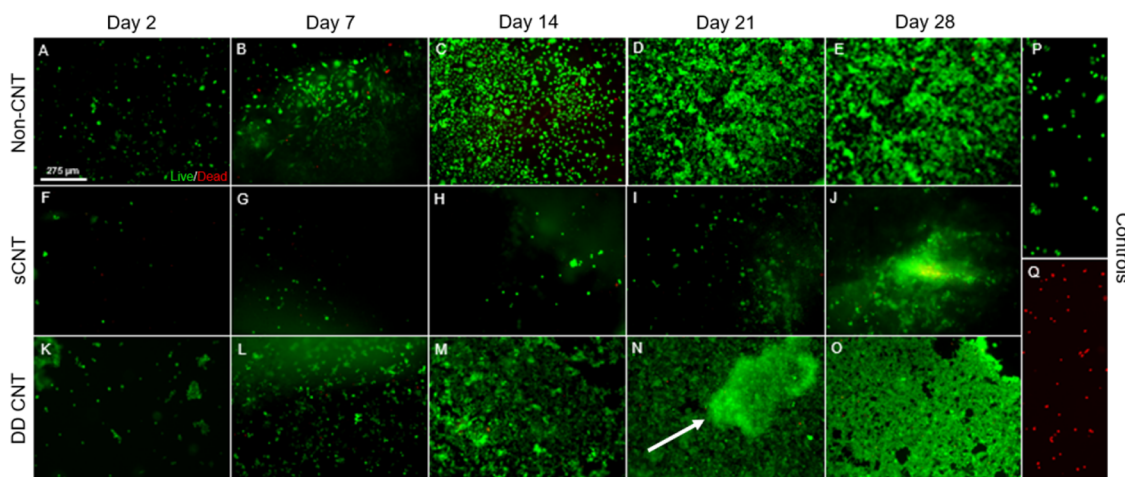
control). On day 5, there was a significant difference between groups, with the DD CNT scaffolds exhibiting the highest cell viability (2909.11 RFU), followed by non-CNT scaffolds (2709.78 RFU), and the cell-only control (2571.00 RFU), with sCNT scaffolds (2146.78 RFU) exhibiting the lowest cell

Figure 8. Cytocompatibility of scaffolds with NIH 3T3 cells. LIVE/DEAD assays of non-CNT, sCNT, and DD CNT scaffolds on day 2 (A, F, K), 7 (B, G, L), 14 (C, H, M), 21 (D, I, N), and 28 (E, J, O). Live stained green and dead stained red with cells-only live (P) and dead (Q) controls. Scale bars = 275 μm.
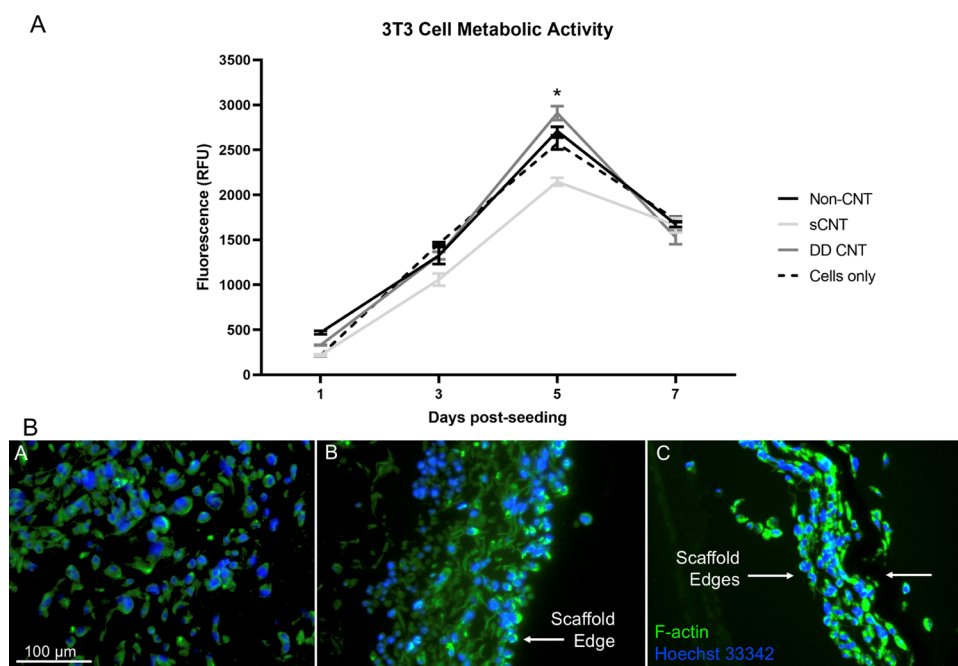
Figure 9. (A) Metabolic activity over 1 week as quantified by Alamar blue assays and (B) phalloidin-stained F-actin filaments green and Hoechst 33342-stained nuclei blue on (A) non-CNT, (B) sCNT, and (C) DD CNT scaffolds. Scale bars = 100 μm. *Denotes $p < 0.05$ significant difference between timepoints. Black = non-CNT, light gray = sCNT, and dark gray = DD CNT.
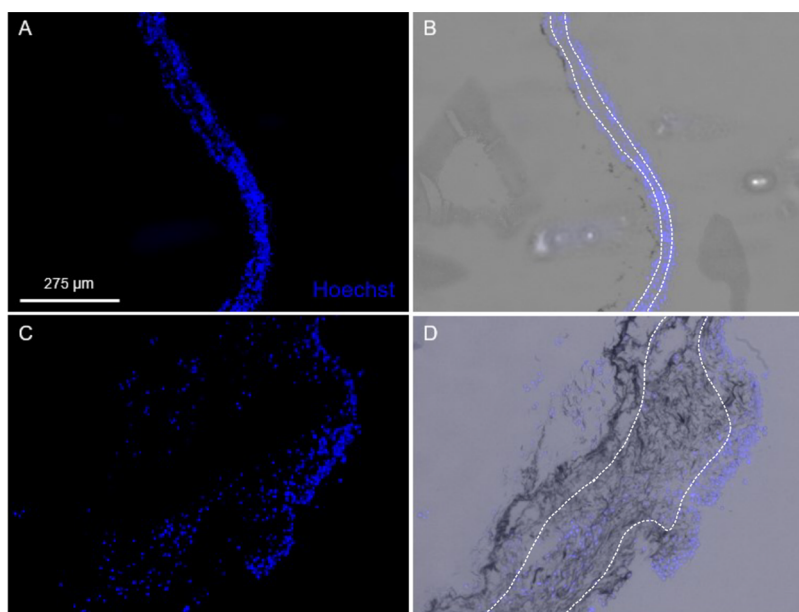

Figure 10. NIH 3T3 migration into scaffolds. Hoechst 33342-stained nuclei of 3T3 cells on day 7 post seeding on cross sectioned sCNT (A, B) and DD CNT (C, D) scaffolds, merged with trans-fluorescent microscope images of scaffolds (B, D). Dotted lines separate the outer 25% of scaffolds from the inner 50%. Scale bars = 275 μm.

highly electrically conductive properties of CNTs. Electrospinning operates through the application of a high voltage to a polymer droplet as it is extruded through a syringe needle. When the electrostatic forces overcome the surface tension forces of the droplet, a charged jet erupts. The jet deposits onto a negatively charged or grounded collector as the solvent simultaneously evaporates, generating a dried, fibrous mat.[31] The deposition of electrospun fibers depends on the electrostatic attraction between the charged jet and the collection plate. In the "sandwich" and dual deposition fabrication methods, CNTs were present in the scaffolds

upon which fibers were electrospun. Thus, we hypothesize that the high electrical conductance of the scaffolds increased electrostatic attraction between the charged jet and the surface of collection, resulting in increased fiber diameter. The charged surface area of the fibers wound around the mandrel contributed to this effect.

We hypothesize that the significant increase in mean pore size when CNTs were incorporated into the scaffolds is also due to electrostatic processes during electrospinning. The increase in pore size was due to increased electrostatic repulsion between formerly and newly deposited electrospun

Table 3. Mean Values ± Standard Error of the Mean For Morphological, Electrical, and Mechanical Data for Each Scaffold Type

	non-CNT	sCNT	DD CNT
volume percent of CNTs (%)	$0.00 \pm 0.00^{a,c}$	$26.39 \pm 2.05^{a,b}$	$51.75 \pm 5.66^{b,c}$
mean fiber diameter (μm)	$1.05 \pm 0.02^{a,c}$	$20.01 \pm 0.92^{a,b}$	$39.53 \pm 3.92^{b,c}$
mean pore size (μm^2)	$9.70 \pm 1.30^{a,c}$	$618.27 \pm 70.77^{a,b}$	$9778.36 \pm 1041.83^{b,c}$
parallel conductance (kS)	0.00 ± 0.00^{c}	0.54 ± 0.10^{b}	$5.22 \pm 0.49^{b,c}$
orthogonal conductance (kS)	0.00 ± 0.00^{c}	0.25 ± 0.003^{b}	$2.85 \pm 1.12^{b,c}$
Young's modulus (MPa)	$6.47 \pm 0.16^{a,c}$	$19.76 \pm 1.95^{a,b}$	$59.32 \pm 6.40^{b,c}$
failure load (kN)	$0.13 \pm 0.012^{a,c}$	0.33 ± 0.0002^{a}	0.36 ± 0.016^{c}
degradation rate (1- fastest)	1	2	3
water contact angle (°)	$73.2 \pm 0.9^{a,c}$	$143.9 \pm 1.2^{a,b}$	$103.9 \pm 1.0^{b,c}$

[a]Denotes $p < 0.05$ significant difference between non-CNT and sCNT. [b]Denotes $p < 0.05$ significant difference between sCNT and DD CNT. [c]Denotes $p < 0.05$ significant difference between non-CNT and DD CNT.

fibers containing CNTs. Additionally, the increased pore size could be due to the less efficient packing of fibers because of their increased volume and decreased quantity.

Inclusion of CNTs also increased the mechanical robustness of the electrospun scaffolds, as shown by their significant increase in Young's modulus (Figure 4C) and failure load (Figure 4D, Table 3). We previously found that decellularized ECM from cardiac tissues of porcine hearts exhibits average Young's moduli of 5.36 ± 0.14 kPa from the left ventricle and 16.69 ± 0.32 kPa from the sinoatrial node.[60] Jacot et al. discovered that Young's modulus of healthy cardiac tissues harvested from the left ventricles of neonatal Black Swiss mice was in the range of 10−15 kPa.[61] While the former data lacks cellular influence on elastic properties, focusing only on the contribution of the ECM, and the latter reference refers to nonhuman, nonadult cardiac tissues, it is likely that Young's modulus of healthy adult cardiac tissues remains in the range of 5−20 kPa due to the extreme physiological similarity between porcine and human hearts.

Our scaffolds, with Young's moduli of 8.33 MPa (non-CNT), 19.76 ± 1.95 MPa (sCNT), and 74.67 MPa (DD CNT) greatly exceed this 10−15 kPa range by several orders of magnitude. Upon initial observation, this could appear problematic; however, high Young's moduli are attractive for their durability, and many materials commonly implanted into cardiovascular tissues have Young's moduli far exceeding that of native cardiac tissues and are mechanically tolerated without issue. For example, vascular grafts comprising commercial expanded polytetrafluoroethylene (ePTFE) exhibit Young's modulus of 17.4 MPa.[62] Commercial sutures commonly used in cardiac bioprostheses exhibit even higher Young's moduli, ranging from 2,315.30 MPa in Gore-Tex to 13.06 GPa in Vicryl. A review by Li et al. reported that Young's moduli of polymers used in implantable prosthetic heart valves are mostly in the range of 10−100 MPa, with one outlier (ePTFE) exhibiting a modulus of 413 MPa.[63] Because these vascular grafts, sutures, and synthetic valves are commonly used and FDA-approved and have Young's moduli similar to or exceeding those of our scaffolds, it is unlikely that the discrepancy in Young's moduli, though large, would have any negative effect within our intended uses both as *in vitro* platforms for the electrophysiological maturation of hiPSC-CMs or as *in vivo* engineered cardiac tissue scaffolds for implantation.

Increased Young's moduli could also appear problematic for neural tissue engineering, particularly considering that softer substrates with lower Young's moduli are typically preferred in

these applications.[64] However, previous research has shown that CNT-based electrospun scaffolds not only show no cytotoxicity toward rat mesenchymal stem cells but actively enhance their proliferation and neural differentiation. These electrospun thermoplastic urethane scaffolds loaded with MWCNTs at 1.5, 2.5, and 3.5% concentrations exhibited Young's moduli of 3.94, 10.01, and 9.80 MPa, respectively, lower but in the same order of magnitude as our CNT-based scaffolds' Young's moduli.[44] Even neuronal stem cells cultured directly onto CNTs exhibited neurite elongation and physiological maturation when electrically stimulated.[42] These results indicate that the robust mechanical properties of CNTs do not impede cell attachment, proliferation, and maturation in neural tissue engineering constructs. Hence, it is unlikely that the increase in Young's modulus due to CNT incorporation will preclude our scaffolds from being used in neural tissue engineering applications.

Inclusion of CNTs by the "sandwich" and dual deposition methods significantly increased the failure load of the scaffolds. The respective mean failure loads of 0.13 ± 0.012, 0.33 ± 0.0002, and 0.38 ± 0.016 kN for the non-CNT, sCNT, and DD CNT scaffolds (Figure 4C) become 0.325 ± 0.03, 0.825 ± 0.0005, and 0.95 ± 0.04 N/mm^2, respectively, when the scaffold area is accounted for, which far exceed the 2−4 mN/mm^2 contractile force exerted by healthy, adult CMs *in vivo*,[8] indicating that there should be no issue with material failure and the scaffolds would tolerate contraction of attaching CMs *in vivo*. The scaffolds are predicted to also tolerate iPSC-CMs with similar (although immature) contractile physiology seeded onto them *in vitro* for electrophysiological maturation. As the neural tissue is noncontractile, withstanding contractile force is a nonissue for most neural tissue engineering applications.

Both mean dry (Figure 5A) and wet (Figure 5B) weights indicate that non-CNT scaffolds degrade the fastest, followed by sCNT, and then DD CNT scaffolds (Table 3). Thus, we conclude that the inclusion of CNTs slows the overall degradation profile of the electrospun PCL−gelatin scaffolds. This is confirmed by SEM images showing CNT arrays remaining intact as PCL and gelatin fibers degrade (Figure 5C). The CNTs remained present longer in DD CNT than sCNT scaffolds due to the higher volume percent of CNTs (Table 1). This difference in the degradation profile between the PCL−gelatin fibers and the CNTs is attractive for *in vivo* applications because it offers the possibility of CNTs remaining to facilitate electrophysiological conduction while PCL−gelatin fibers degrade and are replaced by *de novo* native tissues. The

degradation profile of the fibers can be tailored by modifying the ratio of PCL to gelatin to match the rate of *de novo* tissue formation for the tissue type of interest.

Inclusion of CNTs into electrospun PCL−gelatin scaffolds significantly increased their water contact angle (Figure 6, Table 3). This indicates that the CNTs are hydrophobic and endow the scaffolds with surface hydrophobicity. The effect is greater for sCNT scaffolds than for DD CNT scaffolds, resulting in significantly higher mean water contact angles. We hypothesize that this is because of the difference in thickness of the outermost layer of electrospun fibers between sCNT and DD CNT scaffolds. Although the volume percent of CNTs is higher in DD CNT scaffolds than in sCNT scaffolds, the electrospun fibers within the sCNT scaffolds are divided into two sections within the "sandwich" structure: above the CNT array and below the CNT array. Thus, though the overall volume percent of electrospun fibers is lower for DD CNT scaffolds, the outermost layer of electrospun fibers that the water droplet interacted with was thicker in the DD CNT scaffolds due to the previously discussed electrostatic effect of the CNTs. This thicker layer of electrospun PCL−gelatin fibers provided a more hydrophilic surface to attenuate the hydrophobicity of the CNTs. Thus, DD CNT scaffolds are more suitable as substrates for mammalian cells, which typically prefer hydrophilic surfaces. This factor likely contributed to the higher proliferation rate on DD CNT than on sCNT scaffolds observed in LIVE/DEAD assays (Figure 8) and higher metabolic activity (Figure 9).

Most notably, CNT incorporation into scaffolds by both the "sandwich" and dual deposition methods significantly increased their end-to-end conductance (Figure 7, Table 3). The CNT-attributed increase in conductance measured greater parallel to the arrayed CNT fibers compared to measurements made in the orthogonal direction. This was observed due to the anisotropy of the conductive network formed by the CNTs. Electrical stimulation has been shown effective in promoting iPSC-CM differentiation[65] and synchronizing the spontaneous beating exhibited by iPSC-CMs,[66] and electrical stimulation of CNTs specifically has been shown to provide cardiomimetic cues to mesenchymal stem cells, directing their differentiation toward CM lineages.[67] Furthermore, electrical stimulation has been shown to facilitate *in vitro* maturation of iPSC-CMs, resulting in increased action potential conduction velocity and calcium ion flux shifting toward physiological values for one study[26] and shifting calcium transients toward physiological values while enhancing membrane N-cadherin signaling, stress-fiber formation, and sarcomeric length shortening when combined with mechanical stimulation in another.[25] The increased electrical conductance of the scaffolds presented in this work potentially offers an attractive substrate for *in vitro* electrophysiological maturation of hiPSC-CMs. Based on our electrical conductance data and results observed in previously mentioned studies, we hypothesize that under the application of electrical stimulation, hiPSC-CMs would exhibit enhanced gap-junctional coupling facilitated by the high electrical conductance of our CNT-based scaffolds, enhancing propagation of action potentials between neighboring hiPSC-CMs and enabling the development of physiologically realistic calcium transients.

Electrical stimulation is also often used in neural tissue engineering. As previously mentioned, researchers cultured neural stem cells onto a rope comprised of single-walled CNTs. The constructs were electrically stimulated 2 days post

seeding. It was concluded based on ENO2 and MECP2 expression that this electrical stimulation promoted the early differentiation of neural stem cells into neurons and the maturation of the neurons post differentiation.[42] A conductive scaffold composed of composite polypyrrole and silk fibroin was found to enhance viability, proliferation, migration, and expression of neurotrophic factors within Schwann cells when electrically stimulated.[68] Due to their high conductance, our CNT-based scaffolds are similarly amenable to electrical stimulation for neural tissue engineering applications.

As previously mentioned, debate exists surrounding whether CNTs are cytocompatible and thus suitable as biomaterials for use in implants or culture systems. Our data indicates that the inclusion of CNTs into our scaffolds results in high cytocompatibility, resulting in negligible cytotoxicity toward NIH 3T3 murine fibroblasts for up to 1 month (Figure 8A) based on fluorescent microscopy of LIVE/DEAD assays and a week-long Alamar blue study done on 3T3 cells (Figure 9). Of the cellular proliferation assays performed on days 1, 3, 5, and 7, the only significant difference in cellular metabolic activity was observed on day 5 (Figure 9). The difference was likely significant on day 5 because this was the timepoint with the highest overall cellular proliferation before contact inhibition caused a decline in metabolic activity. On day 5, DD CNT scaffolds exhibited the highest proliferation, followed by non-CNT scaffolds, the cell-only control, and finally the sCNT scaffolds. We hypothesize that the cells preferred the homogenous microstructure of the DD CNT and non-CNT scaffolds to the heterogeneous microstructure of the sCNT scaffolds. The sCNT scaffolds exhibit more heterogeneity in structure than the DD CNT and non-CNT scaffolds because the layers of CNT arrays and electrospun PCL−gelatin fibers are arranged in a "sandwich" geometry (Figure 2).

Based on both the viability assays (Figure 8) and proliferation assays (Figure 9), cells appeared to prefer DD CNT scaffolds to sCNT scaffolds. In addition to the previously discussed heterogeneity of sCNT scaffolds, scaffold morphology also contributed to this difference. DD CNT scaffolds exhibit significantly greater fiber diameter and pore size than sCNT scaffolds (Table 2), resulting in increased surface area, which allows more attachment and proliferation sites for cells.

Fibroblasts maintained their cellular morphology when seeded onto CNT-based scaffolds, visualized with phalloidin and Hoechst 33342 staining performed on day 14 post seeding (Figure 9C). Finally, fibroblasts migrated into both sCNT and DD CNT scaffolds, traversing their thickness by day 7 post seeding, as shown by phalloidin staining on sectioned cellularized scaffolds (Figure 10). This indicates that the CNT-based scaffolds provide an attractive and biomimetic microenvironment for cellular attachment, proliferation, and migration, the hallmarks of a robust biomaterial for tissue engineering applications. Furthermore, these scaffolds can be used as conductive substrates for the application of electrical stimulation to cells, which has been explored as a method for *in vitro* maturation of hiPSC-CMs[65,66] and neural stem cells.[42]

5. CONCLUSIONS

We here present two types of electrospun, CNT-based scaffolds, which are highly electrically conductive and cytocompatible. The use of electrospinning as a fabrication method allows for easy tunability of the resulting scaffolds, whose morphology can be easily controlled by modifying solution properties and electrospinning parameters. Both the

"sandwich" and dual deposition methods of CNT incorporation are amenable to modifications in the electrospinning portion of the fabrication process.

Due to their increased electrical conductance and high cytocompatibility, these scaffolds hold potential for the development of novel cardiac and neural tissue-engineered constructs. Neural applications include spinal cord and peripheral nerve regeneration, neuronal growth substrates, and microfluidic models of the brain. Cardiac applications include cellular pacemakers, three-dimensional (3D) printed cardiac tissues, and cardiac patches for tissue repair following myocardial infarction. Additionally, these scaffolds show promise for incorporation into *in vitro* platforms to electrophysiologically mature hiPSC-CMs, making them relevant for use in a myriad of cardiac tissue engineering applications.

◼ ASSOCIATED CONTENT

🆂🅸 Supporting Information

The Supporting Information is available free of charge at https://pubs.acs.org/doi/10.1021/acsomega.2c01807.

> Supporting information uploaded separately contains the experimental setup for tensile testing and mean distributions of fiber diameter and pore size for each scaffold type (non-CNT, sCNT, and DD CNT) (PDF)

◼ AUTHOR INFORMATION

Corresponding Author

Jessica M. Gluck − *Department of Textile Engineering, Chemistry, and Science, North Carolina State University, Raleigh, North Carolina 27606, United States;* ◎ orcid.org/0000-0002-6908-0809; Email: jmgluck@ncsu.edu

Authors

Taylor C. Suh − *Department of Textile Engineering, Chemistry, and Science, North Carolina State University, Raleigh, North Carolina 27606, United States;* ◎ orcid.org/0000-0001-6957-3315

Jack Twiddy − *Joint Department of Biomedical Engineering, North Carolina State University and The University of North Carolina at Chapel Hill, Raleigh, North Carolina 27606, United States;* ◎ orcid.org/0000-0003-1929-5796

Nasif Mahmood − *Department of Textile Engineering, Chemistry, and Science, North Carolina State University, Raleigh, North Carolina 27606, United States*

Kiran M. Ali − *Department of Textile Engineering, Chemistry, and Science, North Carolina State University, Raleigh, North Carolina 27606, United States*

Mostakima M. Lubna − *Department of Textile Engineering, Chemistry, and Science, North Carolina State University, Raleigh, North Carolina 27606, United States*

Philip D. Bradford − *Department of Textile Engineering, Chemistry, and Science, North Carolina State University, Raleigh, North Carolina 27606, United States;* ◎ orcid.org/0000-0002-4448-5033

Michael A. Daniele − *Joint Department of Biomedical Engineering, North Carolina State University and The University of North Carolina at Chapel Hill, Raleigh, North Carolina 27606, United States; Department of Electrical and Computer Engineering, North Carolina State University, Raleigh, North Carolina 27606, United States;* ◎ orcid.org/0000-0002-2016-4091

Complete contact information is available at:

https://pubs.acs.org/10.1021/acsomega.2c01807

◼ ACKNOWLEDGMENTS

◼ ABBREVIATIONS

CM, cardiomyocyte; CNT, carbon nanotube; CVD, chemical vapor deposition; DD CNT, dual deposition carbon nanotube; ECM, extracellular matrix; ePTFE, expanded polytetrafluoroethylene; hiPSC, human-induced pluripotent stem cell; hiPSC-CM, human-induced pluripotent stem cell-derived cardiomyocytes; MWCNT, multiwalled carbon nanotube; PCL, polycaprolactone; PEDOT, poly(3,4-ethylenedioxythiophene); sCNT, "sandwich" carbon nanotube

◼ REFERENCES

(1) Ahmad, F. B.; Cisewski, J. A.; Minino, A.; Anderson, R. N. Provisional Mortality Data - United States, 2020. *Morb. Mortal. Wkly. Rep.* **2021**, *70*, 519−522.

(2) Centers for Disease Control and Prevention (CDC). Prevalence of Heart Disease - United States, 2005. *Morb. Mortal. Wkly. Rep.* **2007**, *56*, 113−118.

(3) Stevens, K. R.; Kruetziger, H. L.; Dupras, S. K.; Korte, F. S.; Regnier, M.; Muskheli, V.; Nourse, M. B.; Bendixen, K.; Reinecke, H.; Murry, C. E. Physiological Function and Transplantation of Scaffold-Free and Vascularized Human Cardiac Muscle Tissue. *Proc. Natl. Acad. Sci. U.S.A.* **2009**, *106*, 16568−16573.

(4) Gao, L.; Gregorich, Z. R.; Zhu, W.; Mattapally, S.; Oduk, Y.; Lou, X.; Kannappan, R.; Borovjagin, A. V.; Walcott, G. P.; Pollard, A. E.; Fast, V. G.; Hu, X.; Lloyd, S. G.; Ge, Y.; Zhang, J. Large Cardiac Muscle Patches Engineered From Human Induced-Pluripotent Stem Cell−Derived Cardiac Cells Improve Recovery From Myocardial Infarction in Swine. *Circulation* **2018**, *137*, 1712−1730.

(5) Zhang, Y. S.; Aleman, J.; Arneri, A.; Bersini, S.; Piraino, F.; Shin, S. R.; Dokmeci, M. R.; Khademhosseini, A. From Cardiac Tissue Engineering to Heart-on-a-Chip: Beating Challenges. *Biomed. Mater.* **2015**, *10*, No. 034006.

(6) Gojo, S.; Kyo, S. Cardiac Regenerative Medicine Cellular Therapy and Tissue Engineering: Cellular Therapy and Tissue Engineering. *Circ. J.* **2009**, *73*, A61−A67.

(7) U.S. Department of Health & Human Services. Health Resources and Services Administration: Scientific Registry of Transplant Recepients, 2019.

(8) Iyer, R. K.; Chiu, L. L.; Reis, L. A.; Radisic, M. Engineered Cardiac Tissues. *Curr. Opin. Biotechnol.* **2011**, *22*, 706−714.

(9) Madsen, J. C. Advances in the Immunology of Heart Transplantation. *J. Heart Lung Transplant.* **2017**, *36*, 1299−1305.

(10) Huang, N. F.; Serpooshan, V.; Morris, V. B.; Sayed, N.; Pardon, G.; Abilez, O. J.; Nakayama, K. H.; Pruitt, B. L.; Wu, S. M.; Yoon, Y.; Zhang, J.; Wu, J. C. Big Bottlenecks in Cardiovascular Tissue Engineering. *Commun. Biol.* **2018**, *1*, No. 199.

(11) Tonsho, M.; Michel, S.; Ahmed, Z.; Alessandrini, A.; Madsen, J. C. Heart Transplantation: Challenges Facing the Field. *Cold Spring Harbor Perspect. Med.* **2014**, *4*, No. a015636.

(12) Bechara, S. L.; Judson, A.; Popat, K. C. Template Synthesized Poly(ε-Caprolactone) Nanowire Surfaces for Neural Tissue Engineering. *Biomaterials* **2010**, *31*, 3492−3501.

(13) Lin, C.; Liu, C.; Zhang, L.; Huang, Z.; Zhao, P.; Chen, R.; Pang, M.; Chen, Z.; He, L.; Luo, C.; Rong, L.; Liu, B. Interaction of IPSC-Derived Neural Stem Cells on Poly(L-Lactic Acid) Nanofibrous Scaffolds for Possible Use in Neural Tissue Engineering. *Int. J. Mol. Med.* **2017**, *41*, 697−708.

(14) Gu, X.; Ding, F.; Williams, D. F. Neural Tissue Engineering Options for Peripheral Nerve Regeneration. *Biomaterials* **2014**, *35*, 6143−6156.

(15) de Ruiter, G. C. W.; Spinner, R. J.; Yaszemski, M. J.; Windebank, A. J.; Malessy, M. J. A. Nerve Tubes for Peripheral Nerve Repair. *Neurosurg. Clin. North Am.* **2009**, *20*, 91−105.

(16) Siemionow, M.; Bozkurt, M.; Zor, F. Regeneration and Repair of Peripheral Nerves with Different Biomaterials: Review. *Microsurgery* **2010**, *30*, 574−588.

(17) Mobini, S.; Song, Y. H.; McCrary, M. W.; Schmidt, C. E. Advances in Ex Vivo Models and Lab-on-a-Chip Devices for Neural Tissue Engineering. *Biomaterials* **2019**, *198*, 146−166.

(18) Wang, S.; Guan, S.; Xu, J.; Li, W.; Ge, D.; Sun, C.; Liu, T.; Ma, X. Neural Stem Cell Proliferation and Differentiation in the Conductive PEDOT-HA/Cs/Gel Scaffold for Neural Tissue Engineering. *Biomater. Sci.* **2017**, *5*, 2024−2034.

(19) Hatamzadeh, M.; Najafi-Moghadam, P.; Beygi-Khosrowshahi, Y.; Massoumi, B.; Jaymand, M. Electrically Conductive Nanofibrous Scaffolds Based on Poly(Ethylene Glycol)s-Modified Polyaniline and Poly(ε-Caprolactone) for Tissue Engineering Applications. *RSC Adv.* **2016**, *6*, 105371−105386.

(20) Garrudo, F. F. F.; Chapman, C. A.; Hoffman, P. R.; Udangawa, R. W.; Silva, J. C.; Mikael, P. E.; Rodrigues, C. A. V.; Cabral, J. M. S.; Morgado, J. M. F.; Ferreira, F. C.; Linhardt, R. J. Polyaniline-Polycaprolactone Blended Nanofibers for Neural Cell Culture. *Eur. Polym. J.* **2019**, *117*, 28−37.

(21) Thunberg, J.; Kalogeropoulos, T.; Kuzmenko, V.; Hägg, D.; Johannesson, S.; Westman, G.; Gatenholm, P. In Situ Synthesis of Conductive Polypyrrole on Electrospun Cellulose Nanofibers: Scaffold for Neural Tissue Engineering. *Cellulose* **2015**, *22*, 1459−1467.

(22) Yang, S.; Jang, LindyK.; Kim, S.; Yang, J.; Yang, K.; Cho, S.-W.; Lee, J. Y. Polypyrrole/Alginate Hybrid Hydrogels: Electrically Conductive and Soft Biomaterials for Human Mesenchymal Stem Cell Culture and Potential Neural Tissue Engineering Applications. *Macromol. Biosci.* **2016**, *16*, 1653−1661.

(23) Bruyneel, A. A.; McKeithan, W. L.; Feyen, D. A.; Mercola, M. Will IPSC-Cardiomyocytes Revolutionize the Discovery of Drugs for Heart Disease? *Curr. Opin. Pharmacol.* **2018**, *42*, 55−61.

(24) Lundy, S. D.; Zhu, W.-Z.; Regnier, M.; Laflamme, M. A. Structural and Functional Maturation of Cardiomyocytes Derived from Human Pluripotent Stem Cells. *Stem Cells Dev.* **2013**, *22*, 1991−2002.

(25) Kroll, K.; Chabria, M.; Wang, K.; Häusermann, F.; Schuler, F.; Polonchuk, L. Electro-Mechanical Conditioning of Human IPSC-Derived Cardiomyocytes for Translational Research. *Prog. Biophys. Biophys. Chem.* **2017**, *130*, 212−222.

(26) Nunes, S. S.; Miklas, J. W.; Liu, J.; Aschar-Sobbi, R.; Xiao, Y.; Zhang, B.; Jiang, J.; Massé, S.; Gagliardi, M.; Hsieh, A.; Thavandiran, N.; Laflamme, M. A.; Nanthakumar, K.; Gross, G. J.; Backx, P. H.; Keller, G.; Radisic, M. Biowire: A Platform for Maturation of Human Pluripotent Stem Cell−Derived Cardiomyocytes. *Nat. Methods* **2013**, *10*, 781−787.

(27) Hirt, M. N.; Boeddinghaus, J.; Mitchell, A.; Schaaf, S.; Börnchen, C.; Müller, C.; Schulz, H.; Hubner, N.; Stenzig, J.; Stoehr, A.; Neuber, C.; Eder, A.; Luther, P. K.; Hansen, A.; Eschenhagen, T. Functional Improvement and Maturation of Rat and Human Engineered Heart Tissue by Chronic Electrical Stimulation. *J. Mol. Cell. Cardiol.* **2014**, *74*, 151−161.

(28) Miki, K.; Deguchi, K.; Nakanishi-Koakutsu, M.; Lucena-Cacace, A.; Kondo, S.; Fujiwara, Y.; Hatani, T.; Sasaki, M.; Naka, Y.; Okubo, C.; Narita, M.; Takei, I.; Napier, S. C.; Sugo, T.; Imaichi, S.; Monjo, T.; Ando, T.; Tamura, N.; Imahashi, K.; Nishimoto, T.; Yoshida, Y. ERRγ Enhances Cardiac Maturation with T-Tubule Formation in Human IPSC-Derived Cardiomyocytes. *Nat. Commun.* **2021**, *12*, No. 3596.

(29) Kowalski, W. J.; Garcia-Pak, I. H.; Li, W.; Uosaki, H.; Tampakakis, E.; Zou, J.; Lin, Y.; Patterson, K.; Kwon, C.; Mukouyama, Y.-S. Sympathetic Neurons Regulate Cardiomyocyte Maturation in Culture. *Front. Cell Dev. Biol.* **2022**, *10*, No. 850645.

(30) Kayama, T.; Okamoto, K.; Gao, M.; Ikegaya, Y.; Sasaki, T. Immature Electrophysiological Properties of Human-Induced Pluripotent Stem Cell-Derived Neurons Transplanted into the Mouse Cortex for 7 Weeks. *NeuroReport* **2019**, *30*, 169−173.

(31) Jun, I.; Han, H.-S.; Edwards, J.; Jeon, H. Electrospun Fibrous Scaffolds for Tissue Engineering: Viewpoints on Architecture and Fabrication. *Int J Mol Sci.* **2018**, *19*, No. 745.

(32) Balguid, A.; Mol, A.; van Marion, M. H.; Bank, R. A.; Bouten, C. V. C.; Baaijens, F. P. T. Tailoring Fiber Diameter in Electrospun Poly(ε-Caprolactone) Scaffolds for Optimal Cellular Infiltration in Cardiovascular Tissue Engineering. *Tissue Eng., Part A* **2009**, *15*, 437−444.

(33) Rogina, A. Electrospinning Process: Versatile Preparation Method for Biodegradable and Natural Polymers and Biocomposite Systems Applied in Tissue Engineering and Drug Delivery. *Appl. Surf. Sci.* **2014**, *296*, 221−230.

(34) Wang, C.; Cheng, Y.-W.; Hsu, C.-H.; Chien, H.-S.; Tsou, S.-Y. How to Manipulate the Electrospinning Jet with Controlled Properties to Obtain Uniform Fibers with the Smallest Diameter?— A Brief Discussion of Solution Electrospinning Process. *J. Polym. Res.* **2011**, *18*, 111−123.

(35) Zhang, H.; Zhou, L.; Zhang, W. Control of Scaffold Degradation in Tissue Engineering: A Review. *Tissue Eng., Part B* **2014**, *20*, 492−502.

(36) Nagarajan, S.; Pochat-Bohatier, C.; Balme, S.; Miele, P.; Kalkura, S. N.; Bechelany, M. Electrospun Fibers in Regenerative Tissue Engineering and Drug Delivery. *Pure Appl. Chem.* **2017**, *89*, 1799−1808.

(37) Woodruff, M. A.; Hutmacher, D. W. The Return of a Forgotten Polymer—Polycaprolactone in the 21st Century. *Prog. Polym. Sci.* **2010**, *35*, 1217−1256.

(38) Sajkiewicz, P.; Kołbuk, D. Electrospinning of Gelatin for Tissue Engineering − Molecular Conformation as One of the Overlooked Problems. *J. Biomater. Sci., Polym. Ed.* **2014**, *25*, 2009−2022.

(39) Sheikholeslam, M.; Wright, M. E. E.; Cheng, N.; Oh, H. H.; Wang, Y.; Datu, A. K.; Santerre, J. P.; Amini-Nik, S.; Jeschke, M. G. Electrospun Polyurethane−Gelatin Composite: A New Tissue-

Engineered Scaffold for Application in Skin Regeneration and Repair of Complex Wounds. *ACS Biomater. Sci. Eng.* **2020**, *6*, 505−516.

(40) Salgado, C. L.; Sanchez, E. M. S.; Zavaglia, C. A. C.; Granja, P. L. Biocompatibility and Biodegradation of Polycaprolactone-Sebacic Acid Blended Gels. *J. Biomed. Mater. Res.* **2012**, *100A*, 243−251.

(41) Miller, K.; Hsu, J. E.; Soslowsky, L. J. Materials in Tendon and Ligament Repair. In *Compr. Biomater.*, Elsevier, 2011; pp 257−279.

(42) Huang, Y.-J.; Wu, H.-C.; Tai, N.-H.; Wang, T.-W. Carbon Nanotube Rope with Electrical Stimulation Promotes the Differentiation and Maturity of Neural Stem Cells. *Small* **2012**, *8*, 2869−2877.

(43) Lovat, V.; Pantarotto, D.; Lagostena, L.; Cacciari, B.; Grandolfo, M.; Righi, M.; Spalluto, G.; Prato, M.; Ballerini, L. Carbon Nanotube Substrates Boost Neuronal Electrical Signaling. *Nano Lett.* **2005**, *5*, 1107−1110.

(44) Pouladzadeh, F.; Katbab, A. A.; Haghighipour, N.; Kashi, E. Carbon Nanotube Loaded Electrospun Scaffolds Based on Thermoplastic Urethane (TPU) with Enhanced Proliferation and Neural Differentiation of Rat Mesenchymal Stem Cells: The Role of State of Electrical Conductivity. *Eur. Polym. J.* **2018**, *105*, 286−296.

(45) Mondal, T.; Das, K.; Singh, P.; Natarajan, M.; Manna, B.; Ghosh, A.; Singh, P.; Saha, S. K.; Dhama, K.; Dutt, T.; Bag, S. Thin Films of Functionalized Carbon Nanotubes Support Long-Term Maintenance and Cardio-Neuronal Differentiation of Canine Induced Pluripotent Stem Cells. *Nanomedicine* **2022**, *40*, No. 102487.

(46) Zheng, N.; Fitzpatrick, V.; Cheng, R.; Shi, L.; Kaplan, D. L.; Yang, C. Photoacoustic Carbon Nanotubes Embedded Silk Scaffolds for Neural Stimulation and Regeneration. *ACS Nano* **2022**, *16*, 2292−2305.

(47) Liu, Y.; Liang, X.; Wang, S.; Hu, K. Electrospun Poly(Lactic-Co-Glycolic Acid)/Multiwalled Carbon Nanotube Nanofibers for Cardiac Tissue Engineering. *J. Biomater. Tissue Eng.* **2016**, *6*, 719−728.

(48) Hopley, E. L.; Salmasi, S.; Kalaskar, D. M.; Seifalian, A. M. Carbon Nanotubes Leading the Way Forward in New Generation 3D Tissue Engineering. *Biotechnol. Adv.* **2014**, *32*, 1000−1014.

(49) Pan, L.; Pei, X.; He, R.; Wan, Q.; Wang, J. Multiwall Carbon Nanotubes/Polycaprolactone Composites for Bone Tissue Engineering Application. *Colloids Surf., B* **2012**, *93*, 226−234.

(50) Kang, S.; Pinault, M.; Pfefferle, L. D.; Elimelech, M. Single-Walled Carbon Nanotubes Exhibit Strong Antimicrobial Activity. *Langmuir* **2007**, *23*, 8670−8673.

(51) Aslan, S.; Loebick, C. Z.; Kang, S.; Elimelech, M.; Pfefferle, L. D.; Van Tassel, P. R. Antimicrobial Biomaterials Based on Carbon Nanotubes Dispersed in Poly(Lactic-Co-Glycolic Acid). *Nanoscale* **2010**, *2*, 1789.

(52) Wu, S.; Duan, B.; Lu, A.; Wang, Y.; Ye, Q.; Zhang, L. Biocompatible Chitin/Carbon Nanotubes Composite Hydrogels as Neuronal Growth Substrates. *Carbohydr. Polym.* **2017**, *174*, 830−840.

(53) Shvedova, A.; Castranova, V.; Kisin, E.; Schwegler-Berry, D.; Murray, A.; Gandelsman, V.; Maynard, A.; Baron, P. Exposure to Carbon Nanotube Material: Assessment of Nanotube Cytotoxicity Using Human Keratinocyte Cells. *J. Toxicol. Environ. Health, Part A* **2003**, *66*, 1909−1926.

(54) Cui, H.-F.; Vashist, S. K.; Al-Rubeaan, K.; Luong, J. H. T.; Sheu, F.-S. Interfacing Carbon Nanotubes with Living Mammalian Cells and Cytotoxicity Issues. *Chem. Res. Toxicol.* **2010**, *23*, 1131−1147.

(55) Fujita, K.; Obara, S.; Maru, J. Pulmonary Toxicity, Cytotoxicity, and Genotoxicity of Submicron-Diameter Carbon Fibers with Different Diameters and Lengths. *Toxicology* **2022**, *466*, No. 153063.

(56) Inoue, Y.; Kakihata, K.; Hirono, Y.; Horie, T.; Ishida, A.; Mimura, H. One-Step Grown Aligned Bulk Carbon Nanotubes by Chloride Mediated Chemical Vapor Deposition. *Appl. Phys. Lett.* **2008**, *92*, No. 213113.

(57) Aly, K.; Lubna, M.; Bradford, P. D. Low Density, Three-Dimensionally Interconnected Carbon Nanotube/Silicon Carbide Nanocomposites for Thermal Protection Applications. *J. Eur. Ceram. Soc.* **2021**, *41*, 233−243.

(58) Alberti, K. A.; Xu, Q. Biocompatibility and Degradation of Tendon-Derived Scaffolds. *Regen. Biomater.* **2016**, *3*, 1−11.

(59) Spearman, S. S.; Irin, F.; Ramesh, S.; Rivero, I. V.; Green, M. J.; Harrysson, O. L. A. Effect of Psuedomonas Lipase Enzyme on the Degradation of Polycaprolactone/Polycaprolactone-Polygylcolide Fiber Blended Nanocomposites. *Int. J. Polym. Mater. Polym. Biomater.* **2018**, *68*, 360−367.

(60) Gluck, J. M.; Herren, A. W.; Yechikov, S.; Kao, H. K. J.; Khan, A.; Phinney, B. S.; Chiamvimonvat, N.; Chan, J. W.; Lieu, D. K. Biochemical and Biomechanical Properties of the Pacemaking Sinoatrial Node Extracellular Matrix Are Distinct from Contractile Left Ventricular Matrix. *PLoS One* **2017**, *12*, No. e0185125.

(61) Jacot, J. G.; Martin, J. C.; Hunt, D. L. Mechanobiology of Cardiomyocyte Development. *J. Biomech.* **2010**, *43*, 93−98.

(62) Bouchet, M.; Gauthier, M.; Maire, M.; Ajji, A.; Lerouge, S. Towards Compliant Small-Diameter Vascular Grafts: Predictive Analytical Model and Experiments. *Mater. Sci. Eng. C* **2019**, *100*, 715−723.

(63) Li, R. L.; Russ, J.; Paschalides, C.; Ferrari, G.; Waisman, H.; Kysar, J. W.; Kalfa, D. Mechanical Considerations for Polymeric Heart Valve Development: Biomechanics, Materials, Design and Manufacturing. *Biomaterials* **2019**, *225*, No. 119493.

(64) Even-Ram, S.; Artym, V.; Yamada, K. M. Matrix Control of Stem Cell Fate. *Cell* **2006**, *126*, 645−647.

(65) Hernández, D.; Millard, R.; Sivakumaran, P.; Wong, R. C. B.; Crombie, D. E.; Hewitt, A. W.; Liang, H.; Hung, S. S. C.; Pébay, A.; Shepherd, R. K.; Dusting, G. J.; Lim, S. Y. Electrical Stimulation Promotes Cardiac Differentiation of Human Induced Pluripotent Stem Cells. *Stem Cells Int.* **2016**, *2016*, 1−12.

(66) Hsiao, C.-W.; Bai, M.-Y.; Chang, Y.; Chung, M.-F.; Lee, T.-Y.; Wu, C.-T.; Maiti, B.; Liao, Z.-X.; Li, R.-K.; Sung, H.-W. Electrical Coupling of Isolated Cardiomyocyte Clusters Grown on Aligned Conductive Nanofibrous Meshes for Their Synchronized Beating. *Biomaterials* **2013**, *34*, 1063−1072.

(67) Mooney, E.; Mackle, J. N.; Blond, D. J.-P.; O'Cearbhaill, E.; Shaw, G.; Blau, W. J.; Barry, F. P.; Barron, V.; Murphy, J. M. The Electrical Stimulation of Carbon Nanotubes to Provide a Cardiomimetic Cue to MSCs. *Biomaterials* **2012**, *33*, 6132−6139.

(68) Zhao, Y.; Liang, Y.; Ding, S.; Zhang, K.; Mao, H.; Yang, Y. Application of Conductive PPy/SF Composite Scaffold and Electrical Stimulation for Neural Tissue Engineering. *Biomaterials* **2020**, *255*, No. 120164.